Case Studies in Construction Materials 24 (2026) e06178

Contents lists available at ScienceDirect

Case Studies in Construction Materials

journal homepage: www.elsevier.com/locate/cscm

Case study

Design-based case study of a GFRP-reinforced RC raft foundation for air-core shunt reactors: Electromagnetic compatibility and reinforcement-level environmental-cost indicators

F. Pinna *, F. Mistretta, M.L. Puppio, F. Stochino

Department of Civil and Environmental Engineering and Architecture, University of Cagliari, Via Marengo 2, 09123, Cagliari, Italy

ARTICLE INFO

Keywords:
GFRP reinforcement
Foundation slab
Shunt reactors
EMC
Serviceability
Reinforced concrete foundations

ABSTRACT

This paper presents a design-based real-scale case study of a glass-fiber-reinforced polymer (GFRP) reinforced-concrete raft foundation supporting air-core shunt reactors in a high-voltage electrical installation. The case is characterized by a specific functional constraint: the reinforcement system had to satisfy conventional structural and geotechnical requirements while improving electromagnetic compatibility (EMC) by reducing the risk of interaction with 50 Hz stray magnetic fields generated by the reactors. Because conventional steel reinforcement may form electrically continuous or quasi-continuous conductive paths, the adopted solution used non-metallic, electrically insulating, and non-magnetic GFRP bars. The foundation consists of a 13.0 m × 11.0 m, 0.60 m thick cast-in-place raft reinforced with 12 mm GFRP bars at 150 mm spacing in both orthogonal directions, with local strengthening zones near auxiliary supports. The study presents the design rationale, the main structural and geotechnical verifications, and a simplified order-of-magnitude electromagnetic assessment based on manufacturer clearance requirements and representative conductive-loop calculations. The GFRP solution is then compared with two steel reinforcement alternatives: a like-for-like 12 mm steel mesh at 150 mm spacing and a code-oriented 14 mm steel mesh at 250 mm spacing. The comparison is limited to reinforcement-level indicators, including reinforcement quantity, cradle-to-gate A1–A3 embodied carbon, and material cost. The adopted GFRP layout reduced reinforcement mass by approximately 75% compared with the like-for-like steel solution. Under the adopted emission factors, the reinforcement-related embodied carbon was estimated as 5.77 tCO_2e for GFRP, compared with 14.57 tCO_2e and 13.46 tCO_2e for the two steel alternatives. Conversely, the reinforcement-only material cost was higher for GFRP. The results show that GFRP reinforcement can be a technically suitable option for foundations placed in electromagnetically constrained environments, provided that the conclusions are interpreted within the limits of a project-specific design case study and reinforcement-level environmental and economic assessment.

1. Introduction

Electrical infrastructures associated with nuclear fission power plants include high-voltage switchyards and auxiliary power

* Corresponding author.
E-mail addresses: francesco.pinna4@unica.it (F. Pinna), fmistret@unica.it (F. Mistretta), mariol.puppio@unica.it (M.L. Puppio), fstochino@unica.it (F. Stochino).

https://doi.org/10.1016/j.cscm.2026.e06178
Received 20 March 2026; Received in revised form 4 May 2026; Accepted 26 May 2026
Available online 28 May 2026

systems where inductive devices are routinely installed to support voltage regulation and reactive-power management. In this context, the mechanical integrity and long-term reliability of civil structures supporting electrical equipment are part of the broader safety and robustness envelope addressed by structural and mechanical engineering for nuclear facilities [1–3].

Among inductive devices, air-core shunt reactors, depicted in Fig. 1, represent a common solution for absorbing reactive power under light-load conditions and stabilizing grid voltage. When operating under alternating current, these devices generate time-varying magnetic fields that extend beyond the reactor footprint. The resulting stray field may induce eddy currents or circulating currents in nearby conductive metallic parts, with associated Joule losses, localized heating, and electromagnetic forces. For this reason, application guidelines and manufacturer documentation prescribe minimum magnetic clearances from metallic objects and emphasize the need to avoid closed conductive loops near air-core reactors [4–6].

These mechanisms become directly relevant for reinforced-concrete (RC) foundations, where conventional carbon-steel reinforcement is electrically conductive and ferromagnetic [7]. In practical construction, rebar networks, lap splices, ties, ancillary metallic components, and grounding details may form closed or quasi-closed conductive paths, thereby providing potential loops for electromagnetic induction [8,9]. For high-reliability energy facilities, this introduces an additional functional requirement: reinforcement selection and detailing must be compatible not only with structural and geotechnical design criteria, but also with electromagnetic compatibility (EMC) constraints imposed by the electrical equipment and its installation environment [10–12].

Reinforced-concrete foundations are traditionally designed using steel reinforcement because of its well-established mechanical behavior, ductility, availability, and compatibility with conventional design standards [13–16]. However, in underground and foundation structures, steel reinforcement may be exposed to aggressive environmental conditions, including groundwater, chlorides, wet–dry cycles, and chemically active soils, which can lead to corrosion-related durability problems, increased maintenance requirements, and reduced service life. Over the past two decades, glass-fiber-reinforced polymer (GFRP) bars have emerged as an alternative reinforcement system, mainly because of their corrosion resistance, low density, high tensile strength, and non-metallic nature [17–20].

The use of GFRP reinforcement has been widely investigated in beams, slabs, bridge decks, piles, and water-retaining structures, where experimental and field evidence has demonstrated satisfactory structural performance when the design properly accounts for the specific mechanical characteristics of FRP reinforcement [21–25]. Compared with steel, GFRP bars have a lower elastic modulus and a linear-elastic brittle tensile response; therefore, serviceability limit states, crack-width control, deflection control, bond behavior, and failure-mode management are often more critical than in conventional steel-reinforced concrete. Recent studies on GFRP-reinforced concrete beams have further highlighted the importance of shear-flexure interaction, stirrup spacing, shear reinforcement type, and failure-mode control in members reinforced with GFRP bars and stirrups [26–28]. These findings are relevant because they confirm that GFRP cannot be treated as a direct one-to-one replacement for steel without considering its different stiffness, bond, and failure characteristics.

Life-cycle cost studies have also shown that, despite higher initial material costs, GFRP-reinforced concrete elements may become economically advantageous over long service periods when corrosion-related inspection, repair, and maintenance interventions are considered [29]. Nevertheless, the application of GFRP bars in foundation elements, such as footings, piles, and foundation slabs,

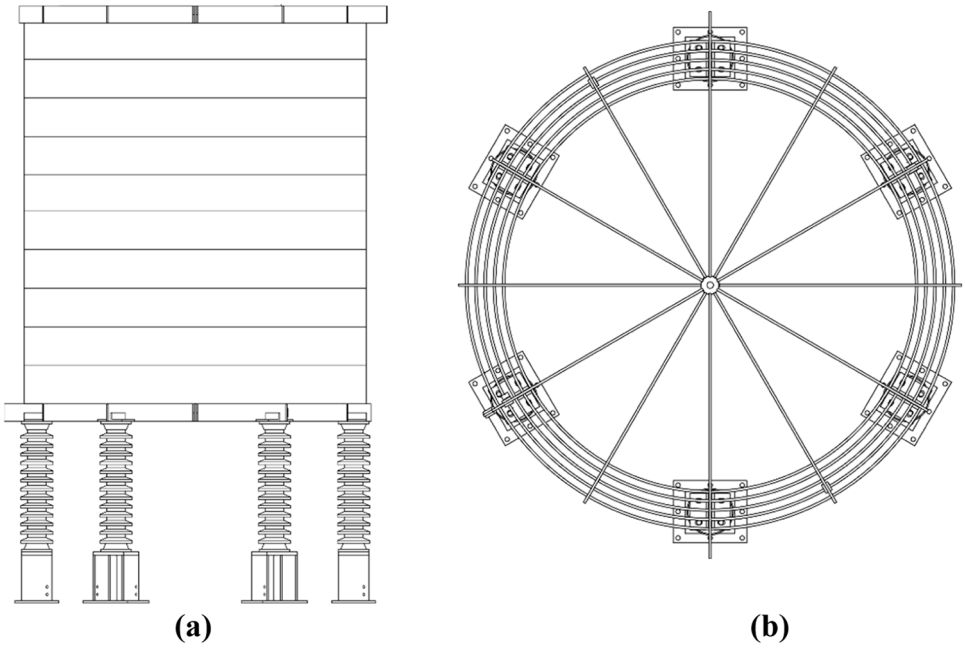

Fig. 1. Air-core shunt reactor: (a) elevation view showing the coil and supporting insulators; (b) plan view of the coil assembly.

remains comparatively limited, and available experimental and field data are still scarce. Several studies have addressed the structural behavior of GFRP-reinforced foundations, with particular emphasis on punching shear, soil–structure interaction, and serviceability response. Full-scale investigations on isolated footings have shown that punching failure in GFRP-reinforced foundations is generally governed by concrete crushing rather than rupture of the FRP reinforcement, with measured bar strains remaining below ultimate values [30–32]. Improvements in punching resistance and deformation capacity have also been reported using shear reinforcement systems, including GFRP shear bands, especially in lightweight-concrete applications [33,34]. Considering serviceability, crack control has been identified as a governing criterion for GFRP-reinforced foundation slabs and slabs-on-ground. Because of the relatively low elastic modulus of GFRP compared with steel, restrained shrinkage, thermal effects, and service loads may lead to wider cracks or larger deflections if the reinforcement ratio and detailing are not properly selected [35]. Long-term field monitoring studies have shown that, although cracks may develop at early age, their widths can remain within code-prescribed limits when the design is governed by serviceability requirements and adequate reinforcement detailing is adopted [36]. Only a limited number of real-scale foundation slab applications reinforced entirely with GFRP bars have been documented in the literature. A notable example is the foundation slab of a 15-storey residential building in Moscow, representing one of the first documented applications of a two-way GFRP-reinforced foundation slab [37]. That study demonstrated the feasibility of designing, constructing, and monitoring massive foundation slabs reinforced with GFRP bars, while also confirming that crack control and local punching resistance may govern the reinforcement demand. Beyond durability and structural serviceability, an additional and still largely unexplored motivation for using GFRP reinforcement in foundations is electromagnetic compatibility. Steel reinforcement may interact with time-varying magnetic fields through two main mechanisms: electrical induction, governed by the induced electromotive force and the effective resistance of closed conductive paths, and magnetic interaction, associated with the ferromagnetic nature of steel and its tendency to perturb the magnetic field. In engineering terms, the relevant quantities are the magnetic flux density, the magnetic flux through a potential conductive loop, the induced electromotive force, the effective loop resistance, the resulting current, and the associated Joule losses. These quantities are directly connected through Faraday's law and Ohm's law, and they provide a rational framework for interpreting why closed metallic loops are restricted in the vicinity of air-core reactors. Interactions between conductive or ferromagnetic components and strong magnetic fields have been documented in large-scale electromagnetic facilities, where magnetic fields may induce additional actions and operational concerns in nearby structural components [38]. GFRP reinforcement changes this interaction mechanism at the material level. Because GFRP bars are non-metallic, electrically insulating, and non-magnetic, they do not provide the same low-resistance conductive paths or ferromagnetic flux-concentration effects associated with steel reinforcement [39,40]. Therefore, the use of GFRP reinforcement can greatly reduce the reinforcement-related electromagnetic interaction pathway and can render induced currents in the reinforcement cage negligible in engineering terms. This does not imply that the entire installation is electromagnetically inert; rather, it means that the reinforcement cage itself is removed as a potential unintended conductive-loop network. Despite the practical relevance of this issue, the current literature on GFRP-reinforced foundations is mainly focused on durability, punching shear, soil–structure interaction, and serviceability performance. To the authors' knowledge, no documented design-based case study has explicitly treated electromagnetic compatibility as a governing design requirement for the selection of reinforcement in a real-scale RC raft foundation supporting inductive electrical equipment. This represents the specific gap addressed in the present work. The paper presents a design-based real-scale case study in which EMC constraints, structural and geotechnical requirements, and reinforcement-level environmental and cost indicators are considered within a single engineering framework. The governing problem can therefore be formulated as follows: a foundation supporting air-core shunt reactors must satisfy conventional structural and geotechnical requirements, including load-bearing capacity, serviceability performance, crack-width control, bearing pressure, settlement compatibility, and stiffness requirements, while also avoiding reinforcement layouts that may form electrically continuous or quasi-continuous conductive loops within the magnetic-clearance region defined by the equipment manufacturer. In this context, the present work addresses a design-based case study in which electromagnetic compatibility acted as a governing requirement for reinforcement selection in a reinforced-concrete raft foundation supporting air-core shunt reactors. The study is framed as a design-based case study combining structural and geotechnical verification, manufacturer clearance requirements, and simplified electromagnetic estimates. It combines the available project design information, structural and geotechnical verifications, manufacturer clearance requirements, and simplified electromagnetic estimates to interpret the role of reinforcement material in an electromagnetically constrained foundation.

The objectives of the study are therefore to: clarify how EMC requirements may influence reinforcement selection in RC foundations supporting inductive electrical equipment; document the design rationale adopted for a GFRP-reinforced raft foundation; summarize the main structural, serviceability, and geotechnical verifications supporting the adopted layout; provide an order-of-magnitude interpretation of the possible induction mechanism in conventional steel reinforcement cages; and compare the adopted GFRP solution with steel reinforcement benchmarks using reinforcement-level mass, cradle-to-gate embodied-carbon, and material-cost indicators. The environmental and economic comparisons are limited to the reinforcement component and are not intended to represent a complete life-cycle assessment or full project-cost analysis.

After this introduction, Section 2 describes the case study and design requirements, including foundation geometry, loading scheme, geotechnical conditions, reinforcement layout, and manufacturer EMC constraints. Section 3 presents the electromagnetic rationale, introducing the mechanisms by which steel reinforcement may interact with stray magnetic fields and the simplified engineering metrics used for order-of-magnitude assessment. Section 4 compares the adopted GFRP solution with two steel reinforcement alternatives in terms of reinforcement quantity and cradle-to-gate embodied-carbon indicators. Section 5 presents the reinforcement-level material-cost comparison. Section 6 discusses the implications and limitations of the design-based case study, and Section 7 summarizes the main conclusions and future research needs.

2. Case study description and design requirements

This case study concerns a design-based real-scale reinforced-concrete raft foundation reinforced with glass-fiber-reinforced polymer (GFRP) bars and intended to support three air-core shunt reactors and their auxiliary components. The supported equipment includes the three main reactors, outdoor current transformers, support insulators, metallic pedestals, anchorage devices, and cable/connection layouts. The foundation was conceived as a cast-in-place RC raft with plan dimensions of 13.00 m × 11.00 m and a thickness of 0.60 m, as shown in Fig. 2(a) and Fig. 2(b). Its function is to transfer the vertical and horizontal actions from the equipment to the subsoil while satisfying structural, geotechnical, serviceability, durability, and electromagnetic compatibility requirements. The adopted concrete strength class is C30/37, with exposure class XC4, corresponding to wet–dry cycles. This selection was made to satisfy durability requirements under the environmental conditions of the site [41]. A nominal concrete cover of 40 mm was adopted

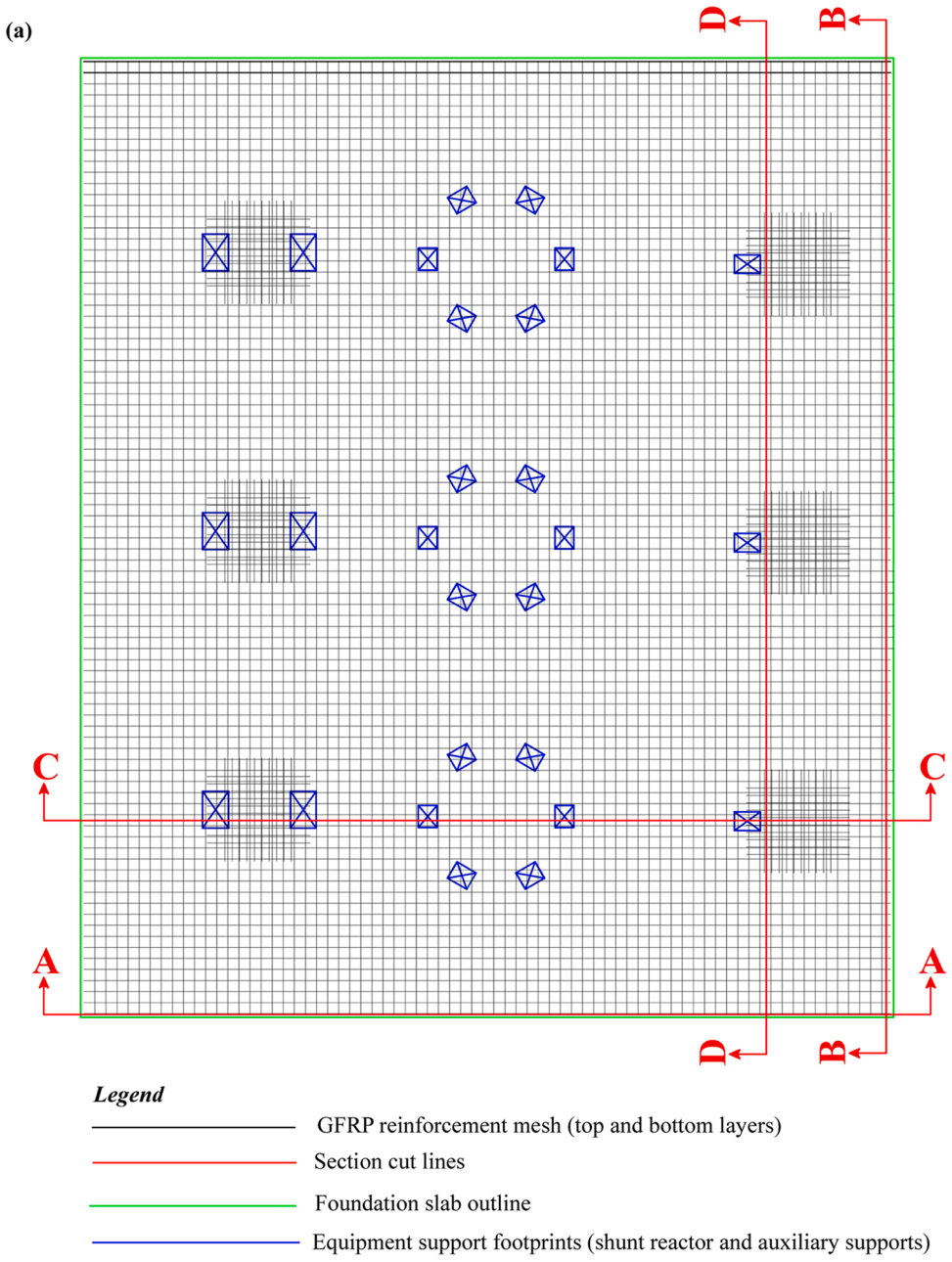

Fig. 2. GFRP-reinforced RC raft foundation supporting three air-core shunt reactors: (a) plan view of the foundation slab showing the orthogonal GFRP reinforcement mesh (top and bottom layers), the slab outline, the equipment footprints, and the section cut lines; (b) longitudinal and transverse sections (A–A, B–B, C–C, D–D) showing overall dimensions and slab thickness.

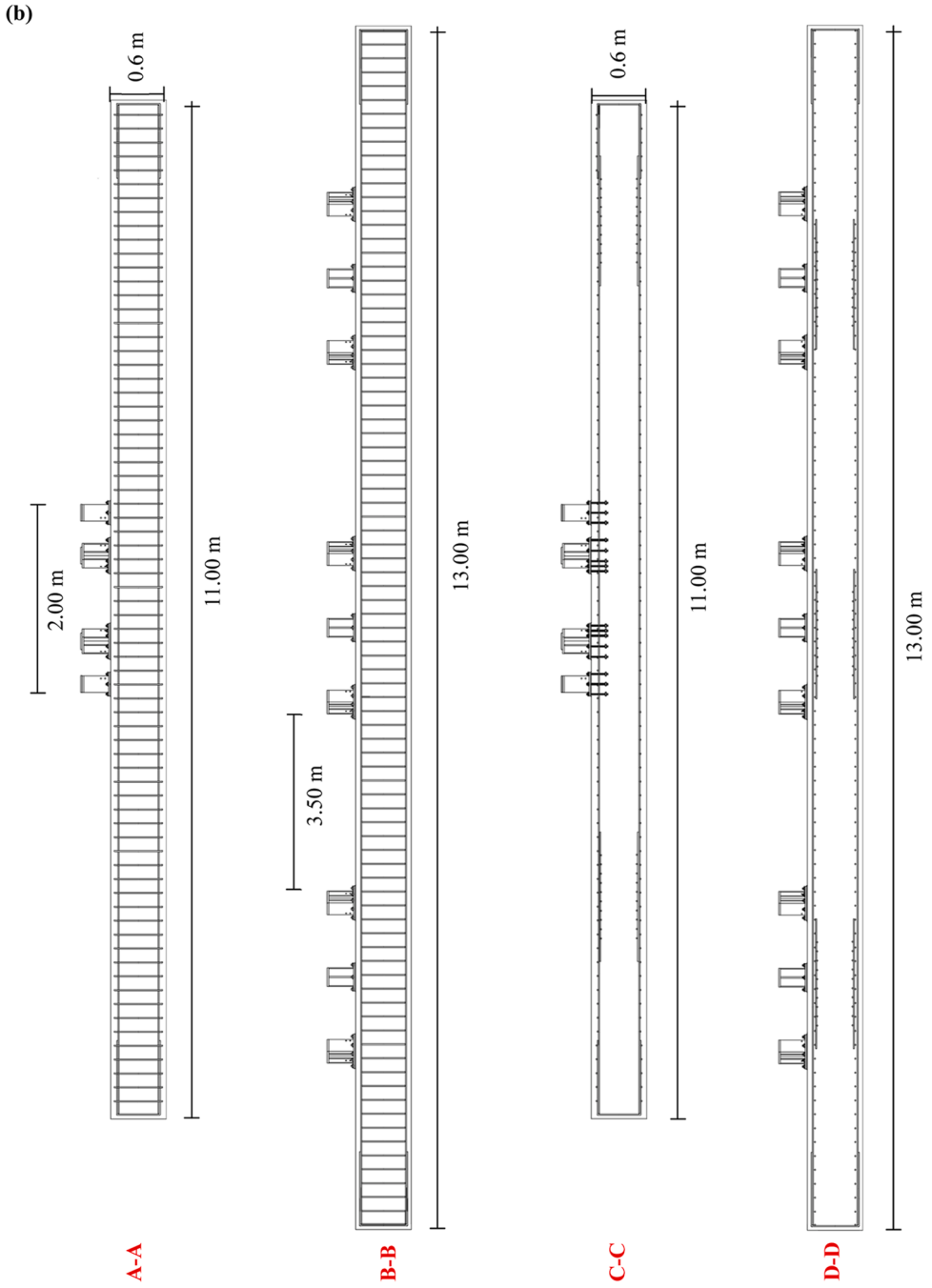

Fig. 2. (*continued*).

for the GFRP reinforcement, consistently with the durability requirements associated with the exposure class. The reinforcement system consists of 12 mm GFRP bars arranged at 150 mm spacing in both orthogonal directions on the top and bottom faces of the raft. Local reinforcement strengthening was also adopted near the support regions of the auxiliary equipment and in zones where load transfer and reinforcement congestion required a denser layout.

The considered shunt reactors are air-core inductive devices operating under alternating-current conditions.

The electrical system is characterized by a voltage of 33 kV and a frequency of 50 Hz, with rated current equal to 140 A, design current equal to 154 A, rated inductance equal to 433.299 mH, and total losses of 32.5 kW per phase at 75°C and rated current. The main geometrical and mass parameters relevant to the structural model are a total reactor height of approximately 3500 mm, an external coil diameter of approximately 2000 mm, and a mass of approximately 1814 kg per coil, increasing to approximately 2151 kg

when the insulators and pedestals are included. The installation layout considered a minimum distance between reactor centerlines of $D_e = 3500$ mm.

The actions transmitted by the equipment to the foundation were defined as reactor-interface design actions. These actions should therefore be interpreted as interface design effects at the base of the individual pedestals, not as the isolated self-weight of the reactor. The summary values adopted at pedestal level are compression $N_{c,Ed} = 17.3$ kN, tension $N_{t,Ed} = 12.1$ kN, shear $T_{Ed} = 4.1$ kN, and bending moment $M_{Ed} = 8.6$ kN·m. These values were applied at the pedestal-foundation interface as concentrated design effects representative of the local load-transfer mechanism. The global model also accounted for the self-weight of the raft, the equivalent mass of the reactors and auxiliary components, wind action, seismic action, and the local effects associated with support and anchorage regions.

The structural design was carried out using a finite-element model of raft and supported equipment. The analysis was performed within the Italian and European design framework, including Eurocode 2 for reinforced concrete checks [41], NTC 2018 [42], Eurocode 1 for wind action [43], Eurocode 7 for geotechnical verification [44], Eurocode 8 for seismic design [45], CNR-DT 203/2006 [46], and the Italian guidelines for the design, qualification, and acceptance of FRP bars for structural use [47]. The load combinations considered ultimate limit states (ULS) and serviceability limit states (SLS), including permanent actions, variable actions, wind action, and seismic effects. The raft was modelled to evaluate the distribution of bending moments, shear forces, and local effects around the equipment support regions.

The reactor–pedestal–raft interface was treated through discrete support regions rather than as a uniformly distributed load. The concentrated actions transferred by the pedestals were applied at the base of the supports, while the local reinforcement strengthening zones were introduced to improve load diffusion around the auxiliary support regions. Twelve local strengthening meshes were considered, six on the top face and six on the bottom face, each with an effective longitudinal extent of approximately 1400 mm. These local reinforcement zones were introduced to account for load transfer, support detailing, and reinforcement congestion near the equipment interfaces.

The adopted GFRP TS12 bars have a nominal diameter of 12 mm, characteristic tensile strength $f_{ft} = 850$ MPa, tensile elastic modulus $E_f = 46$ GPa, partial safety factor $\gamma_m = 1.5$, environmental conversion factor $\eta_a = 0.65$, and long-term conversion factors defined for SLS and ULS verifications. The GFRP stress–strain response was assumed linear elastic up to rupture, consistently with the design assumptions for FRP reinforcement. The effective depth of the reinforced section was evaluated considering the 0.60 m slab thickness, concrete cover, and bar position. The reinforcement ratio was computed as $\rho_f = A_f/(bd)$ for a unit-width strip of the raft, with A_f obtained from the adopted 12 mm bars at 150 mm spacing.

The ULS flexural verification was performed by comparing the design bending moment obtained from the finite-element analysis with the resistant moment of the GFRP-reinforced section. The maximum design bending moment per unit width was $M_{Ed} = 44$ kN·m/m in the most unfavorable direction, while the calculated resistant moment of the adopted GFRP section was $M_{Rd} = 133$ kN·m/m. Therefore, the flexural verification was satisfied with a significant safety margin. The shear verification was also carried out for the GFRP-reinforced section without transverse shear reinforcement. The maximum design shear was $V_{Ed} = 159$ kN/m, while the calculated shear resistance was $V_{Rd} = 201$ kN/m. The shear check was therefore also satisfied. In addition, punching shear around support regions was checked according to the adopted design framework, and the calculated punching resistance was found to be adequate for the support reactions derived from the FEM analysis.

SLS behavior was explicitly considered because the lower elastic modulus of GFRP compared with steel can make crack-width and deformation control more relevant than in conventional steel-reinforced concrete. The serviceability checks included stress limitation, deformation control, and crack-width verification. The crack-width assessment was performed under service conditions using the adopted GFRP reinforcement properties and the service load combinations. The calculated characteristic crack width was approximately $w_k = 0.15$ mm, which is lower than the adopted reference limit for the exposure and reinforcement condition. Therefore, the adopted reinforcement density was not governed only by ultimate strength, but also by serviceability and detailing requirements. The minimum anchorage length of the GFRP bars was also checked and set equal to 800 mm, in accordance with the adopted design procedure.

The wind action on the reactors was evaluated by modelling the reactor body as a cylindrical element. A horizontal wind action of 3.57 kN was adopted at reactor level, corresponding to a reference wind speed of 120 km/h. This value was checked against the wind-action provisions of Eurocode 1 [43]. Considering a cylindrical geometry with diameter approximately equal to 2.0 m and height approximately equal to 3.49 m, the corresponding wind force was found to be consistent with the range obtained from the Eurocode-based assessment, depending on the adopted pressure coefficient and reference wind speed. The value of 3.57 kN was therefore retained as a conservative project input for the structural model.

The geotechnical design was based on the available site investigations, including boreholes, dynamic penetration tests, MASW tests, seismic refraction tests, and electrical resistivity surveys. The subsoil profile is characterized by a shallow layer of vegetal and agricultural soil, extending approximately to 0.3–0.5 m depth, underlain by moderately dense slightly silty sand with gravel extending to at least 15 m depth. The groundwater table was identified at approximately 4.50 m below ground level. The representative soil parameters adopted for the geotechnical assessment include a unit weight in the range of 19–20 kN/m^3 , a friction angle in the range of 32–35°, and elastic modulus values of approximately 1.77–2.94 kN/cm^2 for the listed layers.

The geotechnical checks were carried out according to NTC 2018 [42] and Eurocode 7 [44]. The verification framework included drained bearing capacity, sliding resistance, liquefaction assessment, total settlement, and differential settlement. For bearing capacity, the foundation–soil system was checked according to the adopted geotechnical design approach. Sliding was verified at the foundation base, while settlement and differential settlement checks were performed to ensure compatibility with the supported

equipment and the serviceability requirements of the raft. The raft was therefore not assumed to be adequate only based on its geometry; its structural and geotechnical adequacy was supported by specific design checks.

The manufacturer also specified a dynamic stiffness requirement, indicating that the equipment should be installed on rigid foundations or structures whose lowest resonance frequency exceeds 33 Hz. This requirement was treated as a functional equipment-support constraint associated with the stiffness of the support system, while the structural and geotechnical adequacy of the raft is documented through the design checks summarized above.

In addition to structural and geotechnical requirements, the foundation had to satisfy electromagnetic compatibility constraints. Because air-core reactors generate 50 Hz stray magnetic fields, the manufacturer's installation requirements indicate that nearby metallic parts may experience induced currents, with possible thermal and electrodynamic effects. The same installation requirements distinguish between metallic parts that do not form closed conductive loops and metallic parts that form closed conductive loops. Two corresponding magnetic-clearance distances are provided from the reactor centerline: MC1 for metallic parts not forming closed loops and MC2 for metallic parts forming closed loops. For the present installation, these values are of the order of MC1 = 0.99–1.46 m and MC2 = 1.96–2.36 m, depending on the reference direction reported in the installation drawing.

This distinction is relevant for reinforced-concrete foundations because conventional steel reinforcement cages may create electrically continuous or quasi-continuous conductive paths through bar continuity, laps, ties, contact points, grounding details, and ancillary metallic components. Such paths may behave like closed conductive loops within the magnetic-clearance region. For this reason, reinforcement selection was treated as an electromagnetic compatibility issue in addition to a structural design issue. The use of GFRP reinforcement reduces the reinforcement-related conductive-loop pathway because the bars are non-metallic, electrically insulating, and non-magnetic. Rather, it means that the reinforcement cage itself is removed as a possible unintended conductive-loop network.

3. Electromagnetic rationale and order-of-magnitude assessment

In the present study, the air-core shunt reactors are installed above the RC raft foundation through discrete support points, consisting of insulating columns and metallic pedestals/anchorage hardware, as typically adopted for outdoor high-voltage equipment, as shown in Fig. 3(a) and Fig. 3(b). Although the reactor body is not in direct contact with the concrete, its stray 50-Hz magnetic field extends into the surrounding space and may intercept metallic components located in the foundation region beneath and around the supports. Therefore, reinforcement embedded in RC foundations may interact with electromagnetic fields generated by nearby power equipment through two main mechanisms: electromagnetic induction in electrically conductive materials and magnetization-related field distortion in ferromagnetic materials. The relevance of these mechanisms is governed primarily by two material parameters: the electrical conductivity σ and the relative magnetic permeability μ_r [48,49].

Electrical conductivity σ quantifies the ability of a material to conduct electric current. A high value of σimplies that an induced electric field may drive significant currents if an electrically continuous path is available. Carbon-steel reinforcement is therefore a conductive material at room temperature [50,51]. In principle, continuous or quasi-continuous steel reinforcement meshes may provide conductive paths for induced currents, although the effective electrical behavior of an actual reinforcement cage depends strongly on construction details, contact resistance, lap splices, tie wires, corrosion products, grounding conditions, and possible discontinuities. Corrosion products may also alter effective electrical continuity, since rust generally exhibits high electrical resistance [52]. By contrast, GFRP bars are effectively electrically insulated, depending on the resin system and fiber architecture [41,53]. For

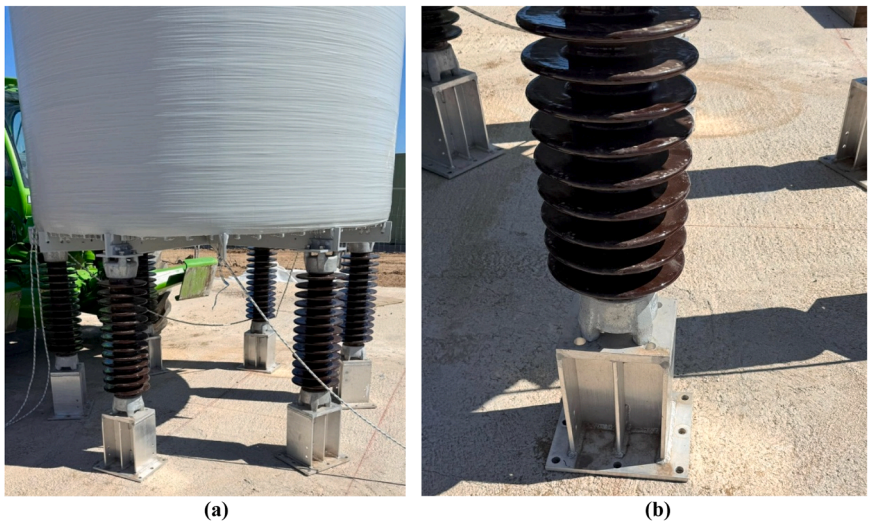

(a) (b)

Fig. 3. Air-core shunt reactor during installation on the reinforced-concrete foundation slab: (a) overall view of the reactor supported by pedestal insulators; (b) close-up of a pedestal base anchorage and support interface on the slab.

engineering purposes, this contrast can be expressed as $\sigma_{steel} \gg 0$ S/m and $\sigma_{GFRP} \approx 0$ S/m, meaning that current circulation may occur in electrically continuous steel paths, whereas it is negligible in GFRP reinforcement.

Relative magnetic permeability μ_r measures the degree to which a material becomes magnetized and modifies the magnetic flux distribution compared with free space [54,55]. Ferromagnetic steels may exhibit $\mu_r \gg 1$, which can promote local magnetic flux concentration and field distortion. By contrast, GFRP is non-magnetic, with $\mu_r \approx 1$; therefore, it does not introduce the same ferromagnetic field-concentration mechanism as steel [56–58].

These differences imply that steel reinforcement can, under appropriate electrical-continuity and field-exposure conditions, provide conductive paths for induced currents and Joule losses, and may also perturb the magnetic field through magnetization effects. Conversely, GFRP reinforcement greatly reduces these reinforcement-related interaction pathways because it is non-metallic, electrically insulating, and non-magnetic. This statement does not imply that the whole foundation system is electromagnetically inert, since metallic anchors, base plates, pedestals, grounding systems, and other ancillary components still require appropriate detailing. A time-varying magnetic flux density $\mathbf{B}(\mathbf{x}, t)$ where $\mathbf{x}$ denotes the spatial position and t the time, generates a non-conservative electric field $\mathbf{E}$ according to the Maxwell–Faraday equation [59]:

$$\nabla \times \mathbf{E} = -\frac{\partial \mathbf{B}}{\partial t} \tag{1}$$

It becomes in integral form over a closed contour $\boldsymbol{C}$ bounding a surface $\boldsymbol{S}$:

$$\oint_C \mathbf{E} \bullet dl = -\frac{d}{dt}\int_S \mathbf{B} \bullet dS = -\frac{d\Phi_{\mathbf{B}}}{dt} \tag{2}$$

Where $\Phi_{\mathbf{B}}$ is the magnetic flux through $\boldsymbol{S}$. Eqs. (1) and (2) formalize the key point: a changing magnetic field creates an electromotive force around any available conductive loop. In RC slabs, closed or quasi-closed conductive paths may arise only if sufficient electrical continuity is provided by the reinforcement layout and by construction details such as bar continuity, lap splices, tie wires, welded points, grounding details, or ancillary metallic elements. In conductive materials, the induced electric field drives current density field through Ohm's law [60]:

$$\mathbf{J} = \sigma \bullet \mathbf{E} \tag{3}$$

Whenever electrical conductivity, σ, is high and electrically continuous paths are available, the electromotive force (emf) can generate circulating currents in the reinforcement network. At the scale of a closed or quasi-closed rebar loop, the mechanism can be interpreted through the circuit-level approximation, where the induced current, I, in the conductive loop is governed by [60,61]:

$$I = -\frac{1}{R_{loop}}\frac{d\Phi_{\mathbf{B}}}{dt} \tag{4}$$

where R_{loop} is the effective resistance of the conductive path. This effective resistance is not only the resistance of the steel bar itself, but may include contact resistances, tie-wire effects, lap-splice behavior, corrosion layers, construction tolerances, and possible discontinuities. Therefore, Eq. (4) should be interpreted as a simplified engineering representation rather than as a direct prediction of the actual current in the constructed foundation. At the local scale, the Joule power density, $p_J = \mathbf{J} \cdot \mathbf{E}$ [62], whereas at the loop scale the total dissipated power, P, is given by:

$$P = I^2 R_{loop} \tag{5}$$

Eqs. (1)–(5) are used here as a simple descriptive model of the induction mechanism. They are intended to show the main physical dependencies of the problem, namely magnetic-field variation, loop area, electrical resistance, induced current, and Joule losses. They are not used as full electromagnetic or thermal verification of the foundation. Such an assessment would require project-specific magnetic-field data and a more detailed electromagnetic–thermal model [63].

A second possible interaction pathway is associated with the ferromagnetic character of steel. Since $\mu_r \gg 1$, steel may locally modify the magnetic-field distribution. In spatially non-uniform magnetic fields, this mechanism may generate magnetic attraction effects on metallic components. However, in the present study, such effects are not introduced as structural loads in the mechanical model, because no calibrated electromagnetic-force evaluation is available. They are mentioned only as part of the physical rationale behind the manufacturer's recommendation to control metallic components and closed conductive loops near air-core reactors.

GFRP reinforcement reduces both reinforcement-related mechanisms at the material level. First, its electrical conductivity is negligible, so Eq. (3) indicates that current circulation within the GFRP reinforcement cage is negligible in engineering terms. Second, GFRP is non-magnetic, so it does not introduce the ferromagnetic flux-concentration mechanism associated with steel. Consequently, for foundations supporting inductive power equipment such as air-core shunt reactors, selecting GFRP reinforcement removes the reinforcement cage from the class of potential metallic conductive-loop networks. The remaining metallic components of the installation, including anchors, pedestals, base plates, and grounding systems, must still be treated through appropriate electromagnetic detailing.

To support this design rationale, an order-of-magnitude estimate was carried out for an idealized steel reinforcement loop. The purpose of this calculation is not to predict the actual induced current in the constructed foundation, but to illustrate the dependence of the induced electrical response on magnetic-field amplitude, loop area, and effective loop resistance [64]. For a time-harmonic magnetic field component normal to the slab the, $B(t) = B_0 \sin(\omega t)$, Faraday's law gives the induced emf around a closed loop of

area A [65]:

$$\varepsilon(t) = -\frac{d\phi_B}{dt} = -A \bullet \omega \bullet B_0 \cos(\omega t) \tag{6}$$

$$\varepsilon_{rms} = \frac{A \bullet \omega \bullet B_0}{\sqrt{2}} \tag{7}$$

where $\Phi_B = A\,B(t)$ is the magnetic flux through the loop and $\omega = 2\pi f$ with $f = 50$ Hz (this because the reactor is connected to the European AC grid). If an electrically continuous steel path exists, the root means square, (rms), loop current can be approximated as [66]:

$$I_{rms} = \frac{\varepsilon_{rms}}{R_{loop}} \tag{8}$$

with R_{loop} the effective electrical resistance of the conductive circuit formed by the reinforcement network (including contact resistances). The corresponding Joule losses scale is:

$$P = I_{rms}^2 \bullet R_{loop} = \frac{\varepsilon_{rms}^2}{R_{loop}} \tag{9}$$

In the considered case study, the manufacturer's installation requirements distinguish between metallic parts that do not form closed loops and metallic parts that form closed loops, defining two corresponding magnetic-clearance regions: MC1 and MC2. For the supplied units, the documented clearances are of the order of MC1 = 1.0–1.5 m and MC2 = 2.0–2.4 m from the coil centerline. These values are not used as direct evidence that embedded reinforcement would necessarily experience critical induction effects. Rather, they are treated as project design constraints indicating that closed conductive metallic paths are a configuration to be avoided near the reactor.

For this reason, a representative idealized loop, shown in Fig. 4, with dimensions comparable to a reactor support bay, was considered.

The assumed loop size is 2.2 × 2.2 m, corresponding to an effective area $A_{\text{eff}} = 4.84$ m^2 and a perimeter $L = 8.8$ m. This geometry is intentionally simplified and does not represent a measured conductive path in the actual foundation. Similarly, the magnetic field is assumed uniform, harmonic, and normal to the loop area. The field around an air-core reactor is three-dimensional, spatially non-uniform, and dependent on the reactor geometry and installation layout. Therefore, local induced voltages may be higher or lower than those obtained from this simplified estimate. A nominal normal stray-field amplitude $B_0 = 1$ mT was adopted as a reference value for illustrating the scaling of the phenomenon. This value is not treated as a measured site-specific field value. Assuming $A_{\text{eff}} = 4.84$ m^2 and $f = 50$ Hz, Eq. (7) gives $\varepsilon_{\text{rms}} = 1.07$ V. Considering a 12 mm diameter carbon-steel bar, a loop perimeter of 8.8 m, and steel conductivity $\sigma = 0.6 \times 10^7$ S/m, corresponding to $\rho = 1.67 \times 10^{-7}$ Ω · m [48], the bar-only resistance is $R_{\text{bar}} = 0.013$ Ω. If the loop resistance were limited to the bar resistance alone, the resulting current would be $I_{\text{rms}} = 82.6$ A and the associated Joule-loss value would be $P = 88.7$ W. This represents an idealized lower-resistance case and should not be interpreted as a realistic prediction for an actual reinforcement cage. To account for the fact that real reinforcement cages include contact resistances, lap splices, tie-wire

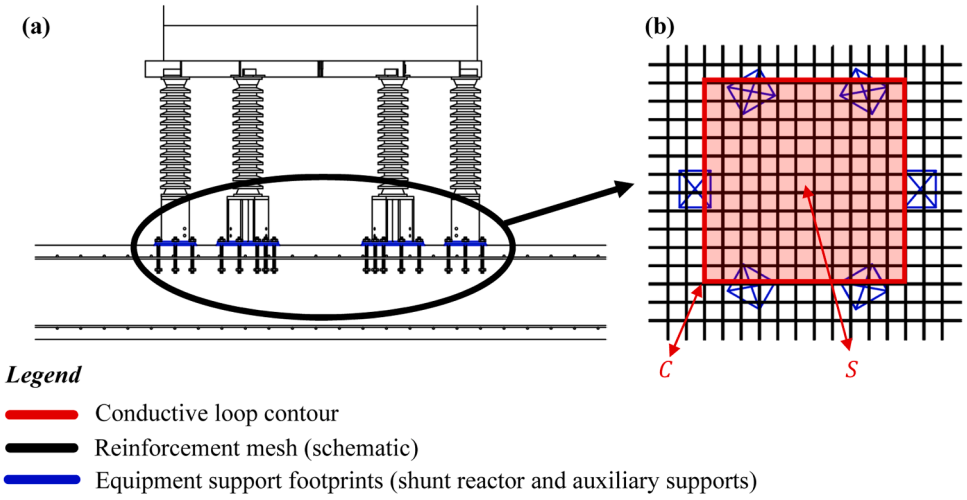

Fig. 4. Schematic representation of a possible closed conductive-loop path in a conventional steel-reinforced foundation below an air-core shunt reactor: (a) reactor support region and raft foundation; (b) plan-view detail of the reinforcement mesh with a representative conductive loop. The highlighted contour represents the integration path C in the integral form of Faraday's law, while the enclosed area defines the magnetic-flux surface S.

connections, possible corrosion products, construction tolerances, grounding details, and discontinuities, an illustrative effective loop-resistance range $R_{loop} = 0.02–0.10\ \Omega$ was also considered. This range is not presented as a measured value, but as a parametric assumption [48–51]. For this range, the estimated current varies from 53.7 A to 10.7 A, while the corresponding Joule-loss value varies from 57.8 W to 11.6 W. If the actual effective resistance is higher, or if the loop is electrically discontinuous, the resulting current would be lower. The main input assumptions and nominal results are summarized in Table 1. The sensitivity of the result follows directly from Eqs. (7)–(9). The induced current scales linearly with B_0, whereas Joule losses scale with B_0^2. Moreover, I_{rms} is inversely proportional to R_{loop}, while P is inversely proportional to R_{loop} for a given induced emf. Therefore, the numerical values in Table 1 should be interpreted as illustrative values for a simplified screening scenario, not as a site-specific electromagnetic or thermal verification. Skin effect, field non-uniformity, concrete cover, and thermal dissipation are not explicitly modelled in this simplified estimate. At 50 Hz, skin effect may influence the effective resistance of ferromagnetic steel depending on magnetic permeability and bar geometry, although this is not represented in the circuit-level calculation. Similarly, concrete cover and surrounding concrete may affect heat dissipation and local boundary conditions, but no temperature-rise calculation is performed in this study. These aspects would require a dedicated coupled electromagnetic–thermal model and are therefore outside the scope of the present design-based case study. This order-of-magnitude check shows that, if a steel cage provides an electrically continuous multi-meter loop, the induced electrical response may become non-negligible at the level of a simplified screening calculation. However, the actual response of a real reinforcement cage may be significantly lower if contact resistances are high or if the conductive path is discontinuous. For this reason, the calculation is not used here to demonstrate a specific thermal or structural risk. Rather, it supports the engineering interpretation of the manufacturer's closed-loop clearance requirement and explains why avoiding metallic reinforcement loops is a rational compatibility-oriented design choice.

In this context, the adopted GFRP reinforcement, shown in Fig. 5, does not provide a comparable metallic conductive-loop network. Therefore, the reinforcement cage itself is removed from the set of components that may fall within the MC2 closed-loop category. Electromagnetic compatibility is thus improved by material selection, while the remaining metallic components of the installation still require appropriate detailing according to the manufacturer's requirements.

4. Reinforcement-level embodied-carbon comparison of GFRP and steel alternatives

Reinforcement selection in raft foundations may influence not only structural detailing and electromagnetic compatibility, but also the embodied carbon associated with material production. In the present study, however, the environmental comparison is intentionally limited to the reinforcement system and to the cradle-to-gate product stage. Therefore, the analysis should not be interpreted as a complete life-cycle assessment of the foundation.

The adopted system boundary includes only modules A1–A3, namely raw-material supply, transport of raw materials to the manufacturer, and manufacturing of the reinforcement product. Transport to site (A4), construction and installation processes (A5), use and maintenance stages (B1–B7), and end-of-life stages (C1–C4) are not included, because project-specific and product-specific data for these stages were not available with comparable reliability for all alternatives. These excluded stages may affect the relative balance between GFRP and steel, particularly because the two materials differ in density, handling requirements, corrosion susceptibility, recyclability, and end-of-life routes. For this reason, the following results are presented as reinforcement-level A1–A3 indicators only.

Concrete-related impacts are also excluded from the comparison. This does not imply that GFRP and steel reinforcement would

Table 1
Nominal induced electrical quantities for a representative closed reinforcement loop under a 50 Hz normal stray magnetic field ($B_0 = 1$ mT).

Quantity	Symbol	Expression	Value	Units
Representative bay size	A_{bs}	2.2×2.2	4.84	m^2
Effective loop area	A_{eff}	2.2×2.2	4.84	m^2
Loop perimeter	L	2.2×4	8.8	m
Steel conductivity	σ	–	0.6×10^7	S/m
Steel resistivity	ρ	$1/\sigma$	1.67×10^{-7}	Ω• m
Bar diameter	d	–	12	mm
Bar cross-sectional area	A_s	$\pi \bullet d^2/4$	1.13×10^{-4}	m^2
Frequency	f	–	50	Hz
Angular frequency	ω	$2 \bullet \pi \bullet f$	314.16	rad/s
Stray-field amplitude	B_0	–	1	mT
Induced rms emf	ε_{rms}	$\omega \bullet B_0 \bullet A_{eff}/\sqrt{2}$	1.07	V
Bar-only resistance	R_{bar}	$\rho \bullet L/A_s$	0.013	Ω
Upper-bound current	I_{rms}	$\varepsilon_{rms}/R_{bar}$	82.6	A
Upper-bound Joule losses	P		88.7	W
Realistic loop resistance (lower bound)	$R_{loop,lb}$	–	0.02	Ω
Current (lower bound)	$I_{rms,lb}$	$\varepsilon_{rms}/R_{loop,lb}$	53.7	A
Joule losses (lower bound)	P_{lb}	$I^2_{rms,lb} \bullet R_{loop,lb}$	57.8	W
Realistic loop resistance (upper bound)	$R_{loop,ub}$	–	0.10	Ω
Current (upper bound)	$I_{rms,ub}$	$\varepsilon_{rms}/R_{loop,ub}$	10.7	A
Joule losses (upper bound)	P_{ub}	$I^2_{rms,ub} \bullet R_{loop,ub}$	11.6	W

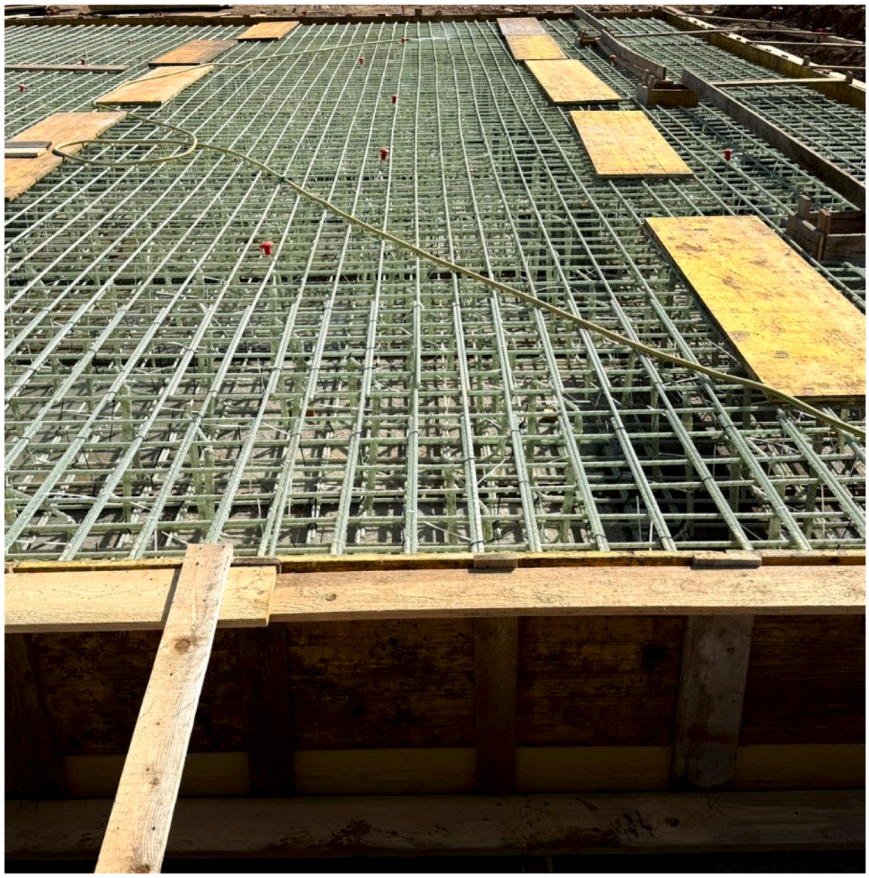

Fig. 5. On-site installation of the GFRP reinforcement cage for the 0.60-m-thick RC raft foundation prior to concrete casting, showing the orthogonal top mesh and detailing over the raft area.

necessarily lead to identical concrete requirements in every optimized design. Rather, the comparison is restricted to the same project geometry, namely the as-built raft dimensions, concrete class, and nominal cover adopted in the case study. A fully functionally equivalent environmental comparison would require redesigning each alternative to satisfy the same ultimate limit state, serviceability limit state, durability, and electromagnetic-compatibility requirements, potentially including changes in slab thickness, crack-width control, cover, reinforcement detailing, and construction assumptions. This broader optimization is outside the scope of the present design-based case study.

Within these boundaries, three reinforcement layouts are compared:

1) The as-built GFRP mesh: 12 mm bars at 150 mm spacing in both orthogonal directions, as implemented in the constructed foundation and depicted in Fig. 6(a). This case represents the adopted design solution, which was verified for the structural and serviceability requirements of the project and selected to satisfy the manufacturer's electromagnetic-compatibility constraints.
2) A like-for-like steel mesh: 12 mm bars at 150 mm spacing in both orthogonal directions. This case is introduced as a material-substitution benchmark at fixed geometry and detailing. It is not intended to represent a fully optimized steel design, but to isolate the effect of replacing GFRP with steel while maintaining the same nominal bar diameter and spacing. This case is not shown separately because it follows the same nominal spacing as the GFRP layout, while differing only in reinforcement material.
3) A code-efficient steel alternative: 14 mm bars at 250 mm spacing in both orthogonal directions. This case represents a coarser steel layout used as a comparative benchmark for reinforcement quantity, embodied carbon, and cost. It should not be interpreted as a fully validated alternative for all project-specific electromagnetic and serviceability constraints, since the presence of steel reinforcement may still require additional electromagnetic detailing to avoid conductive-loop configurations. This configuration is also represented schematically in Fig. 6(b).

The raft plan area is $A_f = 13.0 \times 11.0 = 143\ \mathrm{m}^2$, as shown in Fig. 2. The reinforcement take-off was estimated as the sum of the base orthogonal meshes on both faces, the local strengthening meshes required near auxiliary-equipment support zones, and the spacer/chair elements required to maintain the prescribed cover and separation between reinforcement layers:

$$L_{tot} = L_{base} + L_{local} + L_{chairs} \tag{10}$$

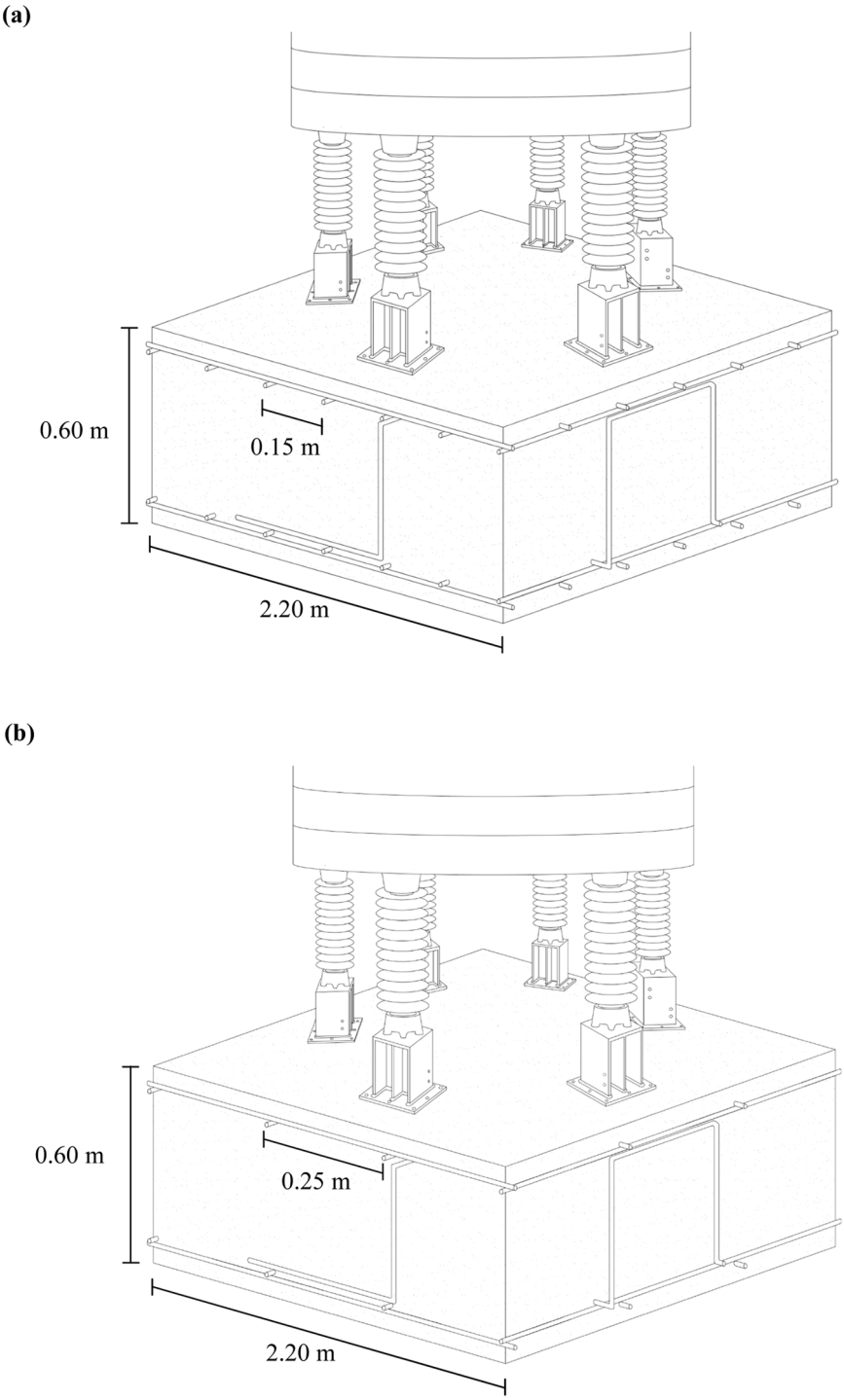

Fig. 6. Schematic view of the raft foundation concept for the air-core shunt reactor and the compared reinforcement layouts: (a) as-built GFRP-reinforced solution with 12 mm bars at 150 mm spacing on both faces; (b) steel alternative adopting a code-efficient mesh (14 mm bars at 250 mm spacing on both faces). The reactor supports pedestals and the corresponding load-transfer zones are shown for reference.

For an orthogonal mesh with spacing s in both directions and reinforcement on both faces, the base bar length is estimated as:

$$L_{base} = \left(\frac{4}{s}\right) \bullet A_f \tag{11}$$

where s is the mesh spacing. This expression represents an idealized quantity take-off based on the nominal project geometry. It does not include all possible cutting waste, construction tolerances, additional laps, hooks, or site-specific detailing losses unless explicitly stated. Therefore, the resulting values should be interpreted as comparative take-off estimates rather than exact procurement quantities.

For the 12 mm bars at 150 mm spacing, Eq. (11) gives $L_{base} \approx 3810$ m. With unit masses $w_{GFRP12} = 0.226$ kg/m and $w_{steel12} = 0.888$ kg/m, the corresponding base-mesh masses are approximately 861 kg for GFRP and 3380 kg for steel. For the 14 mm steel bars at 250 mm spacing, Eq. (11) gives $L_{base} \approx 2290$ m. Adopting $w_{steel14} = 1.21$ kg/m, the corresponding base-mesh mass is approximately 2770 kg.

The reinforcement layout also includes twelve local strengthening meshes, six on the top face and six on the bottom face. Each patch has an effective extent of approximately $a = 1400$ mm, with local spacing $s_{loc} = 100$ mm in both directions. For a square patch $a \times a$, the bar length per patch is estimated as:

$$L_{patch} = 2 \bullet \left[\left(\frac{a}{s_{loc}}\right) + 1\right] \bullet a \tag{12}$$

Using $a = 1400$ mm and $s_{loc} = 100$mm, the number of bars per direction is $n = 15$, and the total additional length associated with the local strengthening meshes is:

$$L_{local} = N_{patch} \bullet L_{patch} \tag{13}$$

Therefore, the total additional reinforcement length associated with the local strengthening meshes is 504 m.

Spacer/chair elements were also included because they are part of the reinforcement support system required to maintain cover and layer separation. The adopted chair density is 12 chairs per square meter in the long direction and 12 chairs per square meter in the short direction, with chair-bar lengths equal to $L_{ch,long} = 1.574$ m and $L_{ch,short} = 1.222$ m, respectively. The corresponding total chair length is:

$$L_{chairs} = A_f \bullet \left(12 \bullet L_{ch,long} + 12 \bullet L_{ch,short}\right) \tag{14}$$

which gives $L_{chairs} \approx 4800$ m for the present foundation. The same nominal spacer/chair length is retained in the comparative take-off for consistency among the three alternatives. However, the actual detailing, material, and quantity of spacer systems may differ between a GFRP and a steel cage; this represents an additional uncertainty of the comparison. The resulting foundation-scale reinforcement quantities are summarized in Table 2. Fig. 7 shows the GFRP reinforcement cage during construction. Values are rounded consistently with the accuracy of the adopted assumptions.

Embodied carbon is estimated to use cradle-to-gate emission factors for the reinforcement component only:

$$m = w \bullet L_{tot} \tag{15}$$

$$CO_2 = m \bullet EF \tag{16}$$

where m is the reinforcement mass, w is the unit mass, L_{tot} is the total reinforcement length, and EF is the cradle-to-gate emission factor expressed in $kgCO_2e/kg$. Published Environmental Product Declarations and EPD-based datasets show that steel-rebar emission factors are strongly dependent on production route, recycled content, and energy mix, with values ranging from low-carbon/high-scrap scenarios to more carbon-intensive industry-average routes [67]. GFRP emission factors are also product-specific and depend on fibre type, resin system, manufacturing process, and electricity mix; values close to 3 $kgCO_2e/kg$ are reported in EPD-based datasets [68].

For baseline comparison, representative factors $EF_{steel} = 1.8$ $kgCO_2e/kg$ and $EF_{GFRP} = 2.8$ $kgCO_2e/kg$ are adopted. Under these assumptions, Eq. (16) gives approximately 5.77 tCO_2e for the as-built GFRP reinforcement, 14.57 tCO_2e for the like-for-like 12 mm steel mesh at 150 mm spacing, and 13.46 tCO_2e for the 14 mm steel mesh at 250 mm spacing. These values are reported in Table 2.

Table 2
Foundation-scale comparison of reinforcement alternatives for the RC mat. Values are reported for representative mid-range emission factors; results are sensitive to supply-chain/EPD assumptions, particularly for steel.

Case	Layout	Spacing s [m]	Total bar length L_{tot} [m]	Unit mass w [kg/m]	Mass m [kg]	Emission factor EF [$kgCO_2e/kg$]	CO_2 [tCO_2e]
1	ϕ12/ 150 mm	0.15	9120	0.226	2060	2.8	5.77
2	ϕ12/ 150 mm	0.15	9120	0.888	8090	1.8	14.57
3	ϕ14/ 250 mm	0.25	7590	1.21	7480	1.8	13.46

Fig. 7. Construction-stage view of the GFRP-reinforced raft foundation prior to concreting, showing the orthogonal reinforcement meshes and the GFRP chairs/spacers used to maintain the required cover and separation between top and bottom layers.

The results show that the adopted GFRP layout substantially reduces reinforcement mass compared with the two steel benchmarks. However, a lower mass does not automatically imply a lower embodied-carbon value, because the environmental indicator depends on the product $m \times EF$. Therefore, the result is sensitive to both reinforcement quantity and emission-factor assumptions.

A simple sensitivity consideration was also added. Under the adopted GFRP emission factor of 2.8 $kgCO_2e/kg$, the GFRP solution provides lower A1–A3 reinforcement-related embodied carbon than the two steel benchmarks only if the steel emission factor is higher than approximately 0.71–0.77 $kgCO_2e/kg$, depending on the steel layout considered. Therefore, if low-carbon/high-scrap steel with product-specific EPD values below this range is available, the carbon advantage of GFRP may decrease or even be reversed. Conversely, for conventional or industry-average steel emission factors around 1.7–1.9 $kgCO_2e/kg$, the lower mass of the GFRP reinforcement offsets its higher emission factor per kilogram.

The environmental comparison should therefore be read as a project-specific reinforcement-level indicator, not as a general statement that GFRP is always environmentally preferable to steel. Under the adopted quantity take-off and emission-factor assumptions, the GFRP solution gives a lower A1–A3 reinforcement-related embodied-carbon value than the two steel benchmarks. However, the result remains dependent on product-specific EPDs, steel production route, recycled content, GFRP fiber and resin system, energy mix, transport distance, installation effort, maintenance scenarios, and end-of-life assumptions. In addition, possible environmental implications associated with electromagnetic mitigation measures for steel cages are not quantified in this study and are therefore not included in the comparison.

5. Reinforcement-level material-cost comparison of GFRP and steel alternatives

Reinforcement choice influences project cost through material price, but also through transport, handling, installation time, lifting requirements, site constraints, maintenance, and end-of-life scenarios. In the present study, however, the economic comparison is intentionally limited to the material cost of the reinforcement system. Therefore, the following estimates should not be interpreted as a complete project-cost assessment or as a life-cycle cost analysis. Labor, transport to site, installation equipment, site productivity, formwork, concrete, excavation, commissioning activities, inspection, maintenance, and end-of-life costs are not included because project-specific data for these items were not available with comparable reliability for all alternatives.

The comparison is carried out at foundation scale using the same three reinforcement layouts considered in Section 4: the as-built GFRP mesh with 12 mm bars at 150 mm spacing in both orthogonal directions; a like-for-like steel mesh with 12 mm bars at 150 mm spacing; and a code-oriented steel benchmark with 14 mm bars at 250 mm spacing. As discussed in Section 4, these alternatives are used as material and detailing benchmarks. They should not be interpreted as fully equivalent solutions in terms of serviceability, durability, installation requirements, and electromagnetic compatibility. A complete equivalent-performance cost comparison would require redesigning each option for the same ULS, SLS, durability, construction, and EMC constraints.

The foundation-scale reinforcement masses m are those reported in Table 2. The reinforcement-only material cost is estimated as:

$$C = m \bullet c \tag{17}$$

where c is the unit material price expressed in €/kg. This €/kg-based approach is used only as a simple and transparent estimate of reinforcement material cost. It does not represent cost per unit structural capacity, cost per unit serviceability performance, or total installed cost. This limitation is relevant because GFRP and steel have different densities, mechanical properties, handling requirements, and installation procedures.

Literature and market practice generally indicate that GFRP bars are more expensive than steel on a mass basis, although the difference can be less pronounced when expressed per installed length because of the lower density of GFRP. For the baseline comparison, representative unit prices are adopted as $c_{steel} = 1.20$ €/kg and $c_{GFRP} = 10.00$ €/kg [69–71]. These values are used as input assumptions for the present case study and should not be interpreted as universal market prices. Actual unit costs may vary depending on supplier, geographic region, procurement volume, bar diameter, resin and fibre system, steel production route, market fluctuations, and contractual conditions. Using Eq. (17), the reinforcement-only material costs are approximately 20.60 k€ for the as-built GFRP mesh, 9.71 k€ for the like-for-like 12 mm steel mesh at 150 mm spacing, and 8.97 k€ for the 14 mm steel mesh at 250 mm spacing. The resulting material-cost comparison is summarized in Table 3.

Under the adopted assumptions, the GFRP solution has a higher reinforcement-material cost than both steel benchmarks. The additional material cost is approximately 10.9 k€ compared with the like-for-like steel mesh and approximately 11.6 k€ compared with the 14 mm at 250 mm steel benchmark. This result is mainly due to the higher unit price of GFRP on a mass basis, which is only partly offset by the lower reinforcement mass.

A simple sensitivity consideration is useful to interpret these values. With the reinforcement quantities adopted in this study, the GFRP unit price would need to be approximately 4.4–4.7 €/kg for the GFRP reinforcement material cost to become comparable with the two steel benchmarks, assuming the steel unit price remains 1.20 €/kg. Conversely, if steel prices increase or if GFRP procurement costs decrease, the difference between the alternatives would become smaller. Therefore, the cost balance should be considered project-specific and dependent on market conditions and procurement assumptions.

The possible economic advantages associated with lower reinforcement weight, easier handling, reduced corrosion susceptibility, and lower maintenance demand are not quantified in this study. These aspects may influence installation cost and life-cycle cost, but their evaluation would require data on installation productivity, labor rates, lifting equipment, transport distance, inspection frequency, repair scenarios, service-life assumptions, discount rate, and end-of-life treatment. For this reason, the present section is limited to a reinforcement-level material-cost comparison. Under the adopted assumptions, GFRP is more expensive in terms of initial reinforcement material cost, while any potential installation or life-cycle cost benefits remain outside the quantified scope of the study.

6. Discussions

The present case study shows that reinforcement selection in foundations supporting air-core shunt reactors cannot be treated only as a conventional structural-material choice. The manufacturer's requirements distinguish between metallic parts that do not form closed conductive loops and metallic parts that may form closed conductive loops, assigning more restrictive magnetic-clearance conditions to the latter. In reinforced-concrete foundations, conventional steel reinforcement cages may potentially create electrically continuous or quasi-continuous paths through bar continuity, laps, tie wires, local contact points, grounding details, or ancillary metallic components. Within this project-specific context, the use of GFRP reinforcement was adopted as a compatibility-oriented design strategy because the reinforcement cage itself is non-metallic, electrically insulating, and non-magnetic. This reduces the reinforcement-related conductive-loop pathway, but it does not imply that the entire installation is electromagnetically inert, since metallic pedestals, anchors, base plates, grounding systems, and other components still require appropriate detailing.

The electromagnetic interpretation presented in this study should therefore be read with its intended scope. The analysis does not provide full site-specific electromagnetic validation, nor does it include measured magnetic-field maps, temperature monitoring, strain measurements, or calibrated Maxwell-based numerical modelling. The order-of-magnitude calculations are used only as a simplified descriptive model to explain why magnetic-field variation, loop area, and effective loop resistance are relevant parameters when conductive loops are present. The calculated currents and Joule losses are not introduced as additional thermal or structural actions in the foundation model. A quantitative prediction of actual induced currents or temperature rise in a steel reinforcement cage would require project-specific magnetic-field data at foundation level, a detailed description of electrical continuity within the reinforcement network, contact resistances, grounding conditions, and a coupled electromagnetic–thermal model.

A more balanced interpretation is also required when comparing GFRP with possible steel alternatives. Steel reinforcement is not intrinsically impossible in electromagnetically constrained environments; in principle, steel cages may be detailed to reduce electromagnetic interaction through segmentation, interruption of closed loops, insulation strategies, controlled grounding, or other project-specific mitigation measures. However, these solutions would require dedicated electromagnetic detailing, verification, and construction control. In the present case, GFRP was selected because it removes the reinforcement cage itself from the class of possible metallic conductive-loop networks, thereby reducing reliance on uncertain assumptions regarding electrical continuity at bar intersections, laps, and ancillary details.

From a structural viewpoint, the adopted GFRP layout was not treated as a simple one-to-one replacement of steel. The lower elastic modulus and linear-elastic brittle behavior of GFRP require explicit attention to serviceability and detailing. For this reason, the design checks reported in the case-study section include flexural resistance, shear resistance, punching verification, anchorage length, and

Table 3
Foundation-scale reinforcement-only material cost comparison (€/kg-based).

Case	Layout	Mass m [kg]	Unit cost c [€/kg]	Reinforcement-only C [k€]
1	ϕ12/150 mm	2060.05	10.00	20.60
2	ϕ12/150 mm	8094.36	1.20	9.71
3	ϕ14/250 mm	7476.60	1.20	8.97

crack-width control. The dense orthogonal mesh on both faces reflects the fact that raft foundations are often governed not only by ultimate resistance but also by serviceability, crack control, load diffusion, and construction detailing. In the present case, the adopted reinforcement layout provided adequate safety margins for the reported design actions and satisfied the serviceability crack-width criterion. Nevertheless, long-term effects such as creep, sustained loading, bond evolution, environmental exposure, and possible cyclic effects were not experimentally monitored in this study and should be considered in future investigations.

The comparison with steel alternatives should also be interpreted within its stated boundaries. The like-for-like steel mesh is a material-substitution benchmark at fixed geometry and detailing, while the 14 mm at 250 mm steel layout is a code-oriented benchmark for reinforcement quantity, embodied carbon, and cost. These alternatives are not presented as fully optimized and experimentally validated designs satisfying all structural, serviceability, durability, installation, and electromagnetic requirements. A complete equivalent-performance comparison would require redesigning each alternative under the same ULS, SLS, durability, construction, and EMC constraints, including possible changes in reinforcement layout, slab detailing, loop interruption measures, and installation procedures.

The environmental comparison is similarly limited. The results refer only to reinforcement-level A1–A3 embodied-carbon indicators and do not represent a complete life-cycle assessment. Under the adopted quantity take-off and emission-factor assumptions, the GFRP solution provides a lower reinforcement-related A1–A3 embodied-carbon value than the two steel benchmarks. However, this result is sensitive to the selected Environmental Product Declarations, steel production route, recycled content, GFRP fiber and resin system, energy mix, and assumed reinforcement quantities. Low-carbon or high-scrap steel documented by product-specific EPDs could reduce or even reverse the carbon advantage observed for GFRP under the baseline assumptions. Therefore, the environmental results should be considered project-specific indicators rather than general evidence that GFRP is always environmentally preferable to steel.

The economic comparison also has a restricted scope. It is limited to reinforcement material cost and does not include labor, transport to site, installation equipment, site productivity, formwork, excavation, concrete, inspection, maintenance, or end-of-life costs. Under the adopted assumptions, the GFRP reinforcement has a higher initial material cost than both steel benchmarks. Possible advantages associated with lower weight, easier handling, corrosion resistance, and reduced maintenance demand are discussed qualitatively but not quantified. Therefore, no complete life-cycle cost conclusion can be drawn from the present study. A full economic assessment would require installation productivity data, labor rates, procurement conditions, maintenance scenarios, discount rate, service-life assumptions, and end-of-life treatment.

Overall, the case study illustrates that GFRP reinforcement can be a technically suitable solution for raft foundations supporting inductive electrical equipment when electromagnetic compatibility is a governing project constraint. The main value of the proposed solution is not that it proves steel reinforcement to be universally unsuitable, but that it demonstrates a practical material-based strategy for reducing the reinforcement-related conductive-loop issue while satisfying the structural and serviceability requirements of the project. Within these limits, the study contributes to the documentation of GFRP-reinforced foundations in electromagnetically constrained installations and highlights the need for future work involving measured 50-Hz magnetic-field maps, coupled electromagnetic–thermal modelling, long-term structural monitoring, product-specific EPDs, and complete life-cycle and life-cycle-cost assessments.

7. Conclusions

This paper presented a design-based real-scale case study of a reinforced-concrete raft foundation for air-core shunt reactors, in which reinforcement selection was governed by both conventional structural requirements and electromagnetic compatibility constraints associated with 50-Hz stray magnetic fields. The study documented the design rationale of the adopted GFRP-reinforced solution, the main structural and geotechnical checks, an order-of-magnitude electromagnetic interpretation of the reinforcement choice, and reinforcement-level environmental and material-cost comparisons with steel benchmarks.

The case study showed that the adopted GFRP reinforcement layout, consisting of 12 mm bars at 150 mm spacing on both faces of a 13.0 m × 11.0 m, 0.60 m thick raft, satisfied the reported ULS and SLS checks. The maximum design bending moment was $M_{Ed} = 44$ kN·m/m, while the calculated resistant moment was $M_{Rd} = 133$ kN·m/m. The maximum design shear was $V_{Ed} = 159$ kN/m, while the calculated shear resistance was $V_{Rd} = 201$ kN/m. The crack-width verification was also satisfied, with a calculated characteristic crack width of approximately $w_k = 0.15$ mm, lower than the adopted reference limit. The anchorage requirement was addressed through a minimum GFRP anchorage length of 800 mm. These results support the structural adequacy of the adopted layout within the design assumptions and project documentation considered in this study.

From the electromagnetic point of view, the manufacturer's requirements distinguish between metallic parts that do not form closed conductive loops (MC1) and metallic parts that may form closed conductive loops (MC2). This assessment does not demonstrate, through field measurements or full electromagnetic modelling, that a specific embedded steel reinforcement cage would necessarily develop critical induced currents or thermal effects. Rather, it shows that conventional steel cages may potentially provide conductive-loop paths if electrical continuity exists through bar continuity, laps, ties, contacts, or ancillary metallic details. In this context, the use of non-metallic, electrically insulating, and non-magnetic GFRP reinforcement reduces the reinforcement-related conductive-loop pathway and removes the reinforcement cage itself from the category of possible metallic loop networks. Metallic anchors, pedestals, base plates, and grounding systems still require appropriate detailing according to the manufacturer's requirements.

The reinforcement-level comparison showed that the adopted GFRP solution reduced reinforcement mass by approximately 75% compared with the like-for-like steel mesh. Under the adopted A1–A3 emission factors, the reinforcement-related embodied carbon was estimated as 5.77 tCO_2e for GFRP, compared with 14.57 tCO_2e for the like-for-like steel mesh and 13.46 tCO_2e for the 14 mm at

250 mm steel benchmark. These values should be interpreted only as reinforcement-level cradle-to-gate indicators, not as a complete life-cycle assessment. The result is sensitive to product-specific Environmental Product Declarations, steel production route, recycled content, GFRP fiber and resin system, energy mix, reinforcement take-off assumptions, transport, installation, maintenance, and end-of-life scenarios.

The material-cost comparison showed the opposite trend. Under the adopted unit prices, the GFRP reinforcement had a higher initial material cost, equal to approximately 20.60 k€, compared with 9.71 k€ for the like-for-like steel mesh and 8.97 k€ for the 14 mm at 250 mm steel benchmark. This comparison is limited to reinforcement material cost and does not include labor, transport, installation equipment, construction productivity, inspection, maintenance, or end-of-life costs. Therefore, no complete project-cost or life-cycle cost conclusion can be drawn from these values.

Overall, within the limits of the design-based case study, GFRP reinforcement proved to be a technically suitable compatibility-oriented solution for the investigated raft foundation. Its main advantage in this project was not a universal superiority over steel, but the ability to satisfy the reported structural and serviceability requirements while reducing the reinforcement-related metallic conductive-loop issue. Steel reinforcement may, in principle, be used with dedicated electromagnetic mitigation measures, such as segmentation, insulation, loop interruption, or controlled grounding strategies; however, such solutions were not designed or quantified in the present study.

The main limitations of the work are the absence of measured magnetic-field maps, thermal monitoring, strain or crack monitoring, and full coupled electromagnetic–thermal modelling. In addition, the environmental comparison is limited to A1–A3 reinforcement indicators, and the economic comparison is limited to reinforcement material cost. Future work should therefore focus on site-specific 50-Hz magnetic-field measurements at foundation level, coupled electromagnetic–thermal modelling of conductive reinforcement cages, long-term monitoring of GFRP-reinforced foundations, product-specific EPD-based assessments, and complete life-cycle and life-cycle-cost analyses.

In a broader perspective, the same compatibility-driven design rationale may be investigated for other reinforced-concrete members placed in electromagnetically demanding environments, such as beams [72,73], columns [74,75], walls [76], and equipment-support substructures. However, dedicated structural, electromagnetic, environmental, and economic analyses would be required before extending the conclusions of the present case study to those applications.

CRediT authorship contribution statement

F. Pinna: Writing – review and editing, Writing – original draft, Methodology, Investigation, Software, Visualization, Validation, Formal analysis. **F.Mistretta:** Writing – review and editing. **M. L. Puppio:** Writing – review and editing. **F. Stochino:** Writing – review and editing, Supervision, Methodology, Conceptualization, Funding acquisition, Project administration, Resources, Validation.

Declaration of Competing Interest

The authors declare that they have no known competing financial interests or personal relationships that could have appeared to influence the work reported in this paper.

Acknowledgements

The authors gratefully acknowledge Maxxi Engineering S.r.l. for providing project information and technical support that enabled the development and documentation of the case study. This work was funded by University of Cagliari under the call ‘Open Access grants: call for applications for contributions to the open access publication 2026.

Data availability

Data will be made available on request.

References

[1] British Standards Institution, Power transformers—Part 6: Reactors (BS EN 60076-6:2008; identical to IEC 60076-6:2007), BSI, 2008.
[2] Council of the European Union, Council Directive 2014/87/Euratom amending Directive 2009/71/Euratom establishing a Community framework for the nuclear safety of nuclear installations, in: Official Journal of the European Union, L 219, 2014, July 8, pp. 42–52.
[3] International Electrotechnical Commission, High-voltage switchgear and controlgear—Part 1: Common specifications for alternating current switchgear and controlgear (IEC 62271-1:2017), IEC, 2017.
[4] S.H. Chang, S.H. Kim, J.Y. Choi, Design of integrated passive safety system (IPSS) for ultimate passive safety of nuclear power plants, Nucl. Eng. Des. 260 (2013) 104–120, https://doi.org/10.1016/j.nucengdes.2013.03.018.
[5] H. Xu, B. Zhang, Y. Liu, New safety strategies for nuclear power plants: A review, Int. J. Energy Res. 45 (8) (2021) 11564–11588, https://doi.org/10.1002/er.6657.
[6] R. Chowdhury, N. Fischer, D. Taylor, D. Caverly, A.B. Dehkordi, A fresh look at practical shunt reactor protection. proceedings of the 49th Annual Western Protective Relay Conference, Spokane, WA, 2022, October.
[7] Y. Lee, S. Lee, G. Kim, H. Eu, M. Son, S. Han, J. Nam, Electrical conductivity and shielding effectiveness of fiber-reinforced cementitious composites according to steel fiber shape, Constr. Build. Mater. 495 (2025) 143497, https://doi.org/10.1016/j.conbuildmat.2025.143497.
[8] H. Wang, C. Gao, Z. Peng, H. Wu, H. Zhao, Z. Guo, Y. Liu, Optimization of airfoil fin PCHE for the power conversion system of lead-based reactor based on reinforcement learning, Nucl. Eng. Des. 421 (2024) 113061, https://doi.org/10.1016/j.nucengdes.2024.113061.

[9] X. Li, S. Cao, E. Yilmaz, Effect of magnetic induction intensity and steel fiber rate on strength improvement of cementitious filling composites, Constr. Build. Mater. 428 (2024) 136417, https://doi.org/10.1016/j.conbuildmat.2024.136417.
[10] J.P. Joule, XVII. On the effects of magnetism upon the dimensions of iron and steel bars, Lond. Edinb. Dublin Philos. Mag. J. Sci. 30 (199) (1847) 76–87.
[11] D. Cecini, S.A. Austin, S. Cavalaro, A. Palmeri, Accelerated electric curing of steel-fibre reinforced concrete, Constr. Build. Mater. 189 (2018) 192–204, https://doi.org/10.1016/j.conbuildmat.2018.08.183.
[12] Y. Jiang, J. Lu, H. Wu, S. Tan, Y. Zhang, X. Cai, Analysis of GFRP insulator characteristics under multiphysical fields in electromagnetic rail launchers, Compos. Struct. 221 (2019) 110900, https://doi.org/10.1016/j.compstruct.2019.110900.
[13] S.H. Kim, W. Choi, Determination of bearing capacity of fiber-reinforced polymer screw piles via field loading tests, Case Stud. Constr. Mater. 22 (2025) e04549, https://doi.org/10.1016/j.cscm.2025.e04549.
[14] D. Zou, B. Liu, Experimental and numerical studies on the impact resistance of reinforced concrete-steel liner composite targets subjected to the tube-type missile impact, Case Stud. Constr. Mater. 23 (2025) e04973, https://doi.org/10.1016/j.cscm.2025.e04973.
[15] A. Prakash, S.A. Priyadharshani, S.V. Rao, Durability and structural integrity of columns reinforced with various combinations of steel and GFRP bars, Case Stud. Constr. Mater. 23 (2025) e05017, https://doi.org/10.1016/j.cscm.2025.e05017.
[16] Y. Tang, S. Zhang, J. Gao, Q. Lu, H. Jiang, Dynamic response of stainless steel-concrete-stainless steel containment structures in nuclear power plants under internal explosions, Nucl. Eng. Des. 448 (2026) 114699, https://doi.org/10.1016/j.nucengdes.2025.114699.
[17] T. Cadenazzi, G. Dotelli, M. Rossini, S. Nolan, A. Nanni, Cost and environmental analyses of reinforcement alternatives for a concrete bridge, Struct. Infrastruct. Eng. 16 (4) (2020) 787–802, https://doi.org/10.1080/15732479.2019.1662066.
[18] A. Elhamaymy, H.M. Mohamed, B. Benmokrane, Durability assessment and behavior under axial load of circular GFRP-RC piles conditioned in severe simulated marine environment, Eng. Struct. 249 (2021) 113376, https://doi.org/10.1016/j.engstruct.2021.113376.
[19] M. Shakiba, H. Ahmadi, S.M.R. Mortazavi, M. Bazli, Z. Azimi, A case study on the feasibility of using static-cast fibre-reinforced concrete electric poles fully reinforced with glass fibre reinforced polymer bars and stirrups, Results Eng. 17 (2023) 100746, https://doi.org/10.1016/j.rineng.2022.100746.
[20] X. Liang, T. Lim, X. Zhao, L. Hu, Q. Yuan, Z. Wang, Novel high-temperature resistant GFRP bars with DOPO-modified vinyl ester: Design, performance, and application, Case Stud. Constr. Mater. 23 (2025) e05022, https://doi.org/10.1016/j.cscm.2025.e05022.
[21] J. Zhou, X. Chen, S. Chen, Durability and service life prediction of GFRP bars embedded in concrete under acid environment, Nucl. Eng. Des. 241 (10) (2011) 4095–4102, https://doi.org/10.1016/j.nucengdes.2011.08.038.
[22] Y. Chang, Y. Wang, B. Li, M. Wang, Z. Zhou, J. Ou, GFRP bar-reinforced seawater sea-sand concrete beam under the combined influence of seawater exposure and sustained load: durability and degradation mechanism, in: Structures, 43, Elsevier, 2022, September, pp. 1503–1515, https://doi.org/10.1016/j.istruc.2022.07.063.
[23] M.T. Elshazli, A. Ibrahim, E. Eidelpes, G.O. Ilevbare, Degradation mechanisms in overpack concrete of spent nuclear fuel dry storage systems: A review, Nucl. Eng. Des. 414 (2023) 112632, https://doi.org/10.1016/j.nucengdes.2023.112632.
[24] T. Liu, H. Kong, Y. Li, J. Wang, M. Wang, X. Chen, Z. Liu, Study on properties of glass fiber filter material for positive zeta potential of coolant in nuclear power plant, Nucl. Eng. Des. 442 (2025) 114203, https://doi.org/10.1016/j.nucengdes.2025.114203.
[25] C. Tai, Y. Yan, D. Zhao, Y. Lu, Experimental research on the flexural behavior of seawater sea-sand ECC composite beams with U-shaped and channel-shaped GFRP profiles as permanent formwork, in: Structures, 82, Elsevier, 2025, December 110491, https://doi.org/10.1016/j.istruc.2025.110491.
[26] N. Oukaili, A.A. Allawi, M.A. Issa, A.I. Said, A. AlBayati, T.H. Ibrahim, G. Wardeh, On the effectiveness of shear reinforcement type in GFRP-reinforced concrete beams: experimental study, Struct. Concr. 26 (5) (2025) 6547–6575, https://doi.org/10.1002/suco.70114.
[27] M.A. Issa, A.A. Allawi, N. Oukaili, Effects of GFRP stirrup spacing on the behavior of doubly GFRP-reinforced concrete beams, Civil. Eng. J. 10 (2) (2024) 502–520, https://doi.org/10.28991/CEJ-2024-010-02-011.
[28] M. AbdulMuttalib Issa, A.A. Allawi, N. Oukaili, Performance of doubly reinforced concrete beams with GFRP bars, J. Mech. Behav. Mater. 33 (1) (2024) 20220308, https://doi.org/10.1515/jmbm-2022-0308.
[29] G. Nkurunziza, A. Debaiky, P. Cousin, B. Benmokrane, Durability of GFRP bars: A critical review of the literature, Progress. Struct. Eng. Mater. 7 (4) (2005) 194–209, https://doi.org/10.1002/pse.205.
[30] L. Nguyen-Minh, M. Rovňák, Punching shear resistance of interior GFRP reinforced slab-column connections, J. Compos. Constr. 17 (1) (2013) 2–13, https://doi.org/10.1061/(ASCE)CC.1943-5614.0000324.
[31] M. Hassan, E. Ahmed, B. Benmokrane, Punching-shear strength of normal and high-strength two-way concrete slabs reinforced with GFRP bars, J. Compos. Constr. 17 (6) (2013) 04013003, https://doi.org/10.1061/(ASCE)CC.1943-5614.0000424.
[32] M. Miralami, M.R. Esfahani, M. Tavakkolizadeh, Strengthening of circular RC column-foundation connections with GFRP/SMA bars and CFRP wraps, Composites Part B Engineering 172 (2019) 161–172, https://doi.org/10.1016/j.compositesb.2019.05.063.
[33] M. Said, M.A. Adam, A.E. Arafa, A. Moatasem, Improvement of punching shear strength of reinforced lightweight concrete flat slab using different strengthening techniques, J. Build. Eng. 32 (2020) 101749, https://doi.org/10.1016/j.jobe.2020.101749.
[34] M.L. Puppio, G. Serra, F. Mistretta, M. Sassu, Anchoring GFRP Rebars: Analysis, Experimental Investigation and Assessment for Design. International Conference of Steel and Composite for Engineering Structures, Springer Nature Switzerland, Cham, 2025, July, pp. 635–642.
[35] C. Mias, L. Torres, M. Guadagnini, A. Turon, Short and long-term cracking behaviour of GFRP reinforced concrete beams, Composites Part B Engineering 77 (2015) 223–231, https://doi.org/10.1016/j.compositesb.2015.03.024.
[36] C. Barris, L. Torres, J. Comas, C. Mias, Cracking and deflections in GFRP RC beams: an experimental study, Composites Part B Engineering 55 (2013) 580–590, https://doi.org/10.1016/j.compositesb.2013.07.019.
[37] V. Kakusha, O. Kornev, M. Kovalev, A. Lapshinov, E. Litvinov, GFRP Reinforced Foundation Slab Design for 15 Story Residential Building, 326, American Concrete Institute, ACI Special Publication, 2018.
[38] O. Mitarai, M. Katsurai, H. Tamura, T. Goto, N. Yanagi, R. Sakamoto, H. Tsutsui, Magnetic interaction between a tokamak reactor and its reinforced-concrete building, Fusion. Eng. Des. 146 (2019) 2057–2061, https://doi.org/10.1016/j.fusengdes.2019.03.101.
[39] C. Viets, S. Kaysser, K. Schulte, Damage mapping of GFRP via electrical resistance measurements using nanocomposite epoxy matrix systems, Composites Part B Engineering 65 (2014) 80–88, https://doi.org/10.1016/j.compositesb.2013.09.049.
[40] K. Yang, Z. Wu, K. Zheng, J. Shi, Shear behavior of regular oriented steel fiber-reinforced concrete beams reinforced with glass fiber polymer (GFRP) bars, in: Structures, 63, Elsevier, 2024, May 106339, https://doi.org/10.1016/j.istruc.2024.106339.
[41] European Committee for Standardization. (2023). Eurocode 2 — Design of concrete structures — Part 1-1: General rules and rules for buildings, bridges and civil engineering structures (EN 1992-1-1:2023).
[42] Ministero delle Infrastrutture e dei Trasporti. (2018). Decreto 17 gennaio 2018: Aggiornamento delle «Norme tecniche per le costruzioni». Gazzetta Ufficiale della Repubblica Italiana, Serie Generale, 42, Supplemento Ordinario n. 8.
[43] European Committee for Standardization. (2005). Eurocode 1 — Actions on structures — Part 1-4: General actions — Wind actions (EN 1991-1-4:2005).
[44] European Committee for Standardization. (2004). Eurocode 7 — Geotechnical design — Part 1: General rules (EN 1997-1:2004).
[45] European Committee for Standardization. (2004). Eurocode 8 — Design of structures for earthquake resistance — Part 1: General rules, seismic actions and rules for buildings (EN 1998-1:2004).
[46] Consiglio Nazionale delle Ricerche. (2006). CNR-DT 203/2006 — Istruzioni per la progettazione, l'esecuzione ed il controllo di strutture di calcestruzzo armato con barre di materiale composito fibrorinforzato.
[47] Consiglio Superiore dei Lavori Pubblici. (2021). Linea guida per l'identificazione, la qualificazione e l'accettazione di barre e staffe in FRP (Fiber Reinforced Polymer), composito fibrorinforzato per uso strutturale.
[48] D.J. Griffiths, Introduction to electrodynamics, Cambridge University Press, 2023.
[49] Hayt, W.H., & Buck, J.A. (2006). Engineering electromagnetics (p. 527). New York.
[50] ASM International. Handbook Committee, Properties and Selection–Irons, Steels, and High-performance Alloys, 1, ASM international, 1990.

[51] W.F. Gale, T.C. Totemeier (Eds.), Smithells metals reference book, Elsevier, 2003.
[52] Z. Hou, Z. Li, J. Wang, Electrically conductive concrete for heating using steel bars as electrodes, J. Wuhan. Univ. Technol. -Mater. Sci. Ed. 25 (3) (2010) 523–526, https://doi.org/10.1007/s11595-010-0035-x.
[53] S. Li, H.H. Tsang, Y. Cheng, Z. Lu, Seismic testing and modeling of cylindrical electrical equipment with GFRP composite insulators, Compos. Struct. 194 (2018) 454–467, https://doi.org/10.1016/j.compstruct.2018.02.036.
[54] L.A.L.E. Landau, E. Lifshitz, On the theory of the dispersion of magnetic permeability in ferromagnetic bodies, Phys. Z. Sowjetunion 8 (153) (1935) 101–114.
[55] E.V. Hristoforou, Permeability sensors for magnetic steel structural health monitoring, Sensors 25 (3) (2025) 606, https://doi.org/10.3390/s25030606.
[56] A.D. Charles, A.N. Rider, S.A. Brown, C.H. Wang, Multifunctional magneto-polymer matrix composites for electromagnetic interference suppression, sensors and actuators, Progress. Mater. Sci. 115 (2021) 100705, https://doi.org/10.1016/j.pmatsci.2020.100705.
[57] K. Katabira, H. Kurita, K. Mori, H. Tamura, F. Narita, Monitoring of Allowable Bending Stress Overload in Glass-Fiber-Reinforced Polymer Composites Using Magnetostrictive Fe–Co Fibers, Adv. Eng. Mater. 26 (4) (2024) 2300529, https://doi.org/10.1002/adem.2023005.
[58] Z. Dong, J. Ji, H. Zhu, J. Chen, M. Yan, D. Zeng, Y. Pan, Flexural behaviour of low-magnetic concrete beams reinforced with ribbed BFRP and/or zero-magnetic steel bars, in: Structures, 76, Elsevier, 2025, June 108973, https://doi.org/10.1016/j.istruc.2025.108973.
[59] P.G. Huray, Maxwell's equations, John Wiley & Sons, 2009.
[60] G.S. Ohm, Die galvanische kette: mathematisch, TH Riemann, 1827.
[61] A.H. Boozer, Ohm's law for mean magnetic fields, J. Plasma Phys. 35 (1) (1986) 133–139.
[62] J.D. Jackson, Classical electrodynamics, John Wiley & Sons, 2021.
[63] Y. Sooriyakanthan, A.J. Gil, P.D. Ledger, M.J. Mallett, High-fidelity modelling of floor-borne vibrations in axisymmetric MRI magnets using hp-finite element method, Comput. Methods Appl. Mech. Eng. 447 (2025) 118385.
[64] H.W. Ott, Electromagnetic compatibility engineering, John Wiley & Sons, 2011.
[65] I. Galili, D. Kaplan, Y. Lehavi, Teaching Faraday's law of electromagnetic induction in an introductory physics course, Am. J. Phys. 74 (4) (2006) 337–343, https://doi.org/10.1119/1.2180283.
[66] J.D. Irwin, R.M. Nelms, Basic engineering circuit analysis, John Wiley & Sons, 2020.
[67] Z. Wang, K. Wang, J. Zhao, S. Wang, E.D. Shumuye, Z. Yang, The mechanical properties of GFRP bars embedded in geopolymer concrete after high temperature exposure, J. Build. Eng. 62 (2022) 105355, https://doi.org/10.1016/j.jobe.2022.105355.
[68] A. Pavlović, T. Donchev, D. Petkova, N. Staletović, Sustainability of alternative reinforcement for concrete structures: Life cycle assessment of basalt FRP bars, Constr. Build. Mater. 334 (2022) 127424, https://doi.org/10.1016/j.conbuildmat.2022.127424.
[69] A. Younis, U. Ebead, S. Judd, Life cycle cost analysis of structural concrete using seawater, recycled concrete aggregate, and GFRP reinforcement, Constr. Build. Mater. 175 (2018) 152–160, https://doi.org/10.1016/j.conbuildmat.2018.04.183.
[70] F. Ascione, G. Maselli, A. Nesticò, Sustainable materials selection in industrial construction: A life-cycle based approach to compare the economic and structural performances of glass fibre reinforced polymer (GFRP) and steel, J. Clean. Prod. 475 (2024) 143641, https://doi.org/10.1016/j.jclepro.2024.143641.
[71] Y. Bai, X. An, G. Wang, H. Rong, Y. Zhang, J. Tao, Seismic performance of short concrete columns reinforced with steel-FRP composite bars and GFRP stirrups, Case Stud. Constr. Mater. (2025) e04703, https://doi.org/10.1016/j.cscm.2025.e0470316/j.nucengdes.2011.08.038.
[72] T. Ülger, M. Cavuslu, Durability and flexural behavior of concrete-filled hybrid GFRP beams with various interface treatments under humid environmental exposure, Case Stud. Constr. Mater. 23 (2025) e04988, https://doi.org/10.1016/j.cscm.2025.e04988.
[73] X. Xi, S. Zhang, Z.H. Hao, P. Feng, F. Zhao, Durability assessment of vacuum-infused GFRP laminates and I-beams in marine environments, Case Stud. Constr. Mater. 22 (2025) e04743, https://doi.org/10.1016/j.cscm.2025.e04988.
[74] M. Noroozolyaee, D. Mostofinejad, A. Saljoughian, A. Zamanvaziri, Behavior of square concrete column reinforced with GFRP bars under new reversed cyclic eccentric loading: Experimental and analytical study, Case Stud. Constr. Mater. (2025) e05598, https://doi.org/10.1016/j.cscm.2025.e05598.
[75] Y. Bai, X. An, G. Wang, H. Rong, Y. Zhang, J. Tao, Seismic performance of short concrete columns reinforced with steel-FRP composite bars and GFRP stirrups, Case Stud. Constr. Mater. 22 (2025) e04703, https://doi.org/10.1016/j.cscm.2025.e04703.
[76] G. Chen, Y. He, J. Liu, C. Mao, Study on the fatigue performance of GFRP connectors in sandwich insulated composite wall panels, Case Stud. Constr. Mater. 22 (2025) e04670, https://doi.org/10.1016/j.cscm.2025.e04670.